Supporting Information:

Magnetic anisotropy and magnetic ordering of

transition-metal phosphorus trisulfides

Tae Yun Kim[*,†,‡,¶] and Cheol-Hwan Park[*,†,‡,¶]

†*Center for Correlated Electron Systems, Institute for Basic Science, Seoul 08826, Korea*

‡*Department of Physics and Astronomy, Seoul National University, Seoul 08826, Korea*

¶*Center for Theoretical Physics, Seoul National University, Seoul 08826, Korea*

E-mail: kimtaeyun@outlook.com; cheolhwan@snu.ac.kr

1   Calculation details: anisotropic magnetic model from constrained DFT+U calculations

1.1   Anisotropic magnetic model

In this section, we describe how the anisotropic magnetic model $H_{\rm tot}$, which is given by

$$H_{\rm tot} = \frac{1}{2} \sum_{i=1}^{N} \sum_{n=1}^{3} \sum_{a=1}^{M_n} \mathbf{S}_i^{\mathsf{T}} \, \mathbf{J}_n^{(a)} \, \mathbf{S}_{j(i,\mathbf{J}_n^{(a)})} + \frac{1}{2} \sum_{i=1}^{N} \sum_{n=1}^{8} \mathbf{S}_i^{\mathsf{T}} \, \mathbf{K}_n \, \mathbf{S}_{j(i,\mathbf{K}_n)}$$
$$+ \sum_{i=1}^{N} \mathbf{S}_i^{\mathsf{T}} \, \mathbf{D} \, \mathbf{S}_i + \sum_{i=1}^{N} \lambda L_{iz} S_{iz} + H_{\rm dip} \, , \tag{S1}$$

where $|\mathbf{S}_i|$ was assumed to be 2.5, 2, and 1 in units of $\hbar$ for MnPS$_3$, FePS$_3$, and NiPS$_3$, respectively, was determined from first-principles calculations. The $C2/m$ symmetry of the crystal structure of TMPS$_3$ was considered to restrict matrices $\mathbf{J}_n^{(a)}$, $\mathbf{K}_n$, and $\mathbf{D}$: (i) $\mathbf{J}_1^{(1)}$, $\mathbf{J}_2^{(1,2)}$, $\mathbf{J}_3^{(1)}$, $\mathbf{K}_1$, $\mathbf{K}_4$, and $\mathbf{D}$ are of

the form

$$\begin{pmatrix} a & 0 & d \\ 0 & b & 0 \\ d & 0 & c \end{pmatrix}, \tag{S2}$$

and (ii) the other matrices in eq S1 are of the form

$$\begin{pmatrix} a & e & d \\ e & b & f \\ d & f & c \end{pmatrix}, \tag{S3}$$

where a, b, c, $\cdots$, and f are real numbers.

Table S1: Calculated on-site parameters (λ and $\mathbf{D}$ in eq S1) in units of meV.

	MnPS$_3$			FePS$_3$			NiPS$_3$		
λ					-10.208				
$\mathbf{D}$	0.000	0.000	0.000	0.029	0.000	-0.003	0.000	0.000	0.003
	0.000	0.000	0.000	0.000	0.000	0.000	0.000	0.005	0.000
	0.000	0.000	0.007	-0.003	0.000	0.064	0.003	0.000	0.113

1.2 Total energy mapping analysis

To obtain the parameters in eq S1, we first calculated the total energies of bilayer TMPS$_3$'s with different magnetic patterns and different collinear directions. Figure S1 shows the collinear magnetic ordering patterns for which DFT+U total energies were calculated. We mention that the lowest-energy configurations obtained from our first-principles calculations coincide with the ordering patterns for all three bulk TMPS$_3$ compounds reported from neutron scattering experiments: the patterns of Figures S1c, g, and f for MnPS$_3$,[S1] FePS$_3$,[S1,S2] and NiPS$_3$,[S3] respectively. For each ordering pattern in Figure S1, six different collinear directions were chosen, which means in total 132 total energy calculations were carried out for *each* TMPS$_3$. With the $C2/m$ symmetry fully considered, the total energies are then used to obtain 73 free parameters for each TMPS$_3$ using the

Table S2: Calculated intralayer exchange parameters ($\mathbf{J}_n^{(a)}$ in eq S1) in units of meV.

	MnPS$_3$	FePS$_3$	NiPS$_3$
$\mathbf{J}_1^{(1)}$	$\begin{pmatrix} 1.065 & 0.000 & -0.001 \\ 0.000 & 1.065 & 0.000 \\ -0.001 & 0.000 & 1.065 \end{pmatrix}$	$\begin{pmatrix} -1.548 & 0.000 & -0.071 \\ 0.000 & -1.197 & 0.000 \\ -0.071 & 0.000 & -1.326 \end{pmatrix}$	$\begin{pmatrix} -5.181 & 0.000 & -0.003 \\ 0.000 & -5.230 & 0.000 \\ -0.003 & 0.000 & -5.220 \end{pmatrix}$
$\mathbf{J}_1^{(2)}$	$\begin{pmatrix} 1.186 & 0.000 & 0.000 \\ 0.000 & 1.186 & 0.001 \\ 0.000 & 0.001 & 1.186 \end{pmatrix}$	$\begin{pmatrix} -1.316 & 0.087 & 0.051 \\ 0.087 & -1.379 & 0.076 \\ 0.051 & 0.076 & -1.371 \end{pmatrix}$	$\begin{pmatrix} -5.345 & 0.020 & 0.001 \\ 0.020 & -5.322 & 0.001 \\ 0.001 & 0.001 & -5.343 \end{pmatrix}$
$\mathbf{J}_1^{(3)}$	$\begin{pmatrix} 1.186 & 0.000 & 0.000 \\ 0.000 & 1.186 & -0.001 \\ 0.000 & -0.001 & 1.186 \end{pmatrix}$	$\begin{pmatrix} -1.316 & -0.087 & 0.051 \\ -0.087 & -1.379 & -0.076 \\ 0.051 & -0.076 & -1.371 \end{pmatrix}$	$\begin{pmatrix} -5.345 & -0.020 & 0.001 \\ -0.020 & -5.322 & -0.001 \\ 0.001 & -0.001 & -5.343 \end{pmatrix}$
$\mathbf{J}_2^{(1,2)}$	$\begin{pmatrix} 0.069 & 0.000 & 0.000 \\ 0.000 & 0.069 & 0.000 \\ 0.000 & 0.000 & 0.070 \end{pmatrix}$	$\begin{pmatrix} 0.106 & 0.000 & -0.005 \\ 0.000 & 0.113 & 0.000 \\ -0.005 & 0.000 & 0.106 \end{pmatrix}$	$\begin{pmatrix} -0.243 & 0.000 & -0.007 \\ 0.000 & -0.233 & 0.000 \\ -0.007 & 0.000 & -0.225 \end{pmatrix}$
$\mathbf{J}_2^{(3,6)}$	$\begin{pmatrix} 0.073 & 0.000 & 0.000 \\ 0.000 & 0.073 & 0.000 \\ 0.000 & 0.000 & 0.073 \end{pmatrix}$	$\begin{pmatrix} 0.120 & 0.008 & 0.002 \\ 0.008 & 0.119 & 0.005 \\ 0.002 & 0.005 & 0.111 \end{pmatrix}$	$\begin{pmatrix} -0.198 & -0.004 & 0.004 \\ -0.004 & -0.203 & 0.006 \\ 0.004 & 0.006 & -0.190 \end{pmatrix}$
$\mathbf{J}_2^{(4,5)}$	$\begin{pmatrix} 0.073 & 0.000 & 0.000 \\ 0.000 & 0.073 & 0.000 \\ 0.000 & 0.000 & 0.073 \end{pmatrix}$	$\begin{pmatrix} 0.120 & -0.008 & 0.002 \\ -0.008 & 0.119 & -0.005 \\ 0.002 & -0.005 & 0.111 \end{pmatrix}$	$\begin{pmatrix} -0.198 & 0.004 & 0.004 \\ 0.004 & -0.203 & -0.006 \\ 0.004 & -0.006 & -0.190 \end{pmatrix}$
$\mathbf{J}_3^{(1)}$	$\begin{pmatrix} 0.721 & 0.000 & 0.000 \\ 0.000 & 0.720 & 0.000 \\ 0.000 & 0.000 & 0.721 \end{pmatrix}$	$\begin{pmatrix} 2.313 & 0.000 & -0.038 \\ 0.000 & 2.372 & 0.000 \\ -0.038 & 0.000 & 2.414 \end{pmatrix}$	$\begin{pmatrix} 27.228 & 0.000 & 0.177 \\ 0.000 & 27.521 & 0.000 \\ 0.177 & 0.000 & 27.390 \end{pmatrix}$
$\mathbf{J}_3^{(2)}$	$\begin{pmatrix} 0.693 & 0.000 & 0.000 \\ 0.000 & 0.693 & 0.000 \\ 0.000 & 0.155 & 0.693 \end{pmatrix}$	$\begin{pmatrix} 2.454 & -0.031 & 0.021 \\ -0.031 & 2.326 & -0.033 \\ 0.021 & -0.133 & 2.427 \end{pmatrix}$	$\begin{pmatrix} 28.221 & 0.126 & -0.089 \\ 0.126 & 28.075 & 0.155 \\ -0.089 & 0.155 & 28.166 \end{pmatrix}$
$\mathbf{J}_3^{(3)}$	$\begin{pmatrix} 0.693 & 0.000 & 0.000 \\ 0.000 & 0.693 & 0.000 \\ 0.000 & 0.155 & 0.693 \end{pmatrix}$	$\begin{pmatrix} 2.454 & 0.031 & 0.021 \\ 0.031 & 2.326 & 0.033 \\ 0.021 & 0.133 & 2.427 \end{pmatrix}$	$\begin{pmatrix} 28.221 & -0.126 & -0.089 \\ -0.126 & 28.075 & -0.155 \\ -0.089 & -0.155 & 28.166 \end{pmatrix}$

Table S3: Calculated interlayer exchange parameters ($\mathbf{K}_n$ in eq S1) in units of meV.

	MnPS$_3$	FePS$_3$	NiPS$_3$
$\mathbf{K}_1$	$\begin{pmatrix} 0.009 & 0.000 & 0.000 \\ 0.000 & 0.009 & 0.000 \\ 0.000 & 0.000 & 0.009 \end{pmatrix}$	$\begin{pmatrix} 0.037 & 0.000 & 0.000 \\ 0.000 & 0.040 & 0.000 \\ 0.000 & 0.000 & 0.039 \end{pmatrix}$	$\begin{pmatrix} -0.048 & 0.000 & -0.001 \\ 0.000 & -0.051 & 0.000 \\ -0.001 & 0.000 & -0.049 \end{pmatrix}$
$\mathbf{K}_2$	$\begin{pmatrix} 0.009 & 0.000 & 0.000 \\ 0.000 & 0.009 & 0.000 \\ 0.000 & 0.000 & 0.009 \end{pmatrix}$	$\begin{pmatrix} 0.041 & 0.000 & 0.000 \\ 0.000 & 0.042 & -0.001 \\ 0.000 & -0.001 & 0.042 \end{pmatrix}$	$\begin{pmatrix} -0.084 & -0.001 & 0.000 \\ -0.001 & -0.083 & -0.002 \\ 0.000 & -0.002 & -0.082 \end{pmatrix}$
$\mathbf{K}_3$	$\begin{pmatrix} 0.025 & 0.000 & 0.000 \\ 0.000 & 0.025 & 0.000 \\ 0.000 & 0.000 & 0.025 \end{pmatrix}$	$\begin{pmatrix} 0.116 & -0.001 & 0.001 \\ -0.001 & 0.112 & -0.002 \\ 0.001 & -0.002 & 0.113 \end{pmatrix}$	$\begin{pmatrix} 1.643 & 0.004 & -0.005 \\ 0.004 & 1.634 & 0.005 \\ -0.005 & 0.005 & 1.639 \end{pmatrix}$
$\mathbf{K}_4$	$\begin{pmatrix} 0.031 & 0.000 & 0.000 \\ 0.000 & 0.031 & 0.000 \\ 0.000 & 0.000 & 0.031 \end{pmatrix}$	$\begin{pmatrix} 0.119 & 0.000 & -0.001 \\ 0.000 & 0.119 & 0.000 \\ -0.001 & 0.000 & 0.119 \end{pmatrix}$	$\begin{pmatrix} 1.626 & 0.000 & 0.006 \\ 0.000 & 1.634 & 0.000 \\ 0.006 & 0.000 & 1.632 \end{pmatrix}$
$\mathbf{K}_5$	$\begin{pmatrix} 0.009 & 0.000 & 0.000 \\ 0.000 & 0.009 & 0.000 \\ 0.000 & 0.000 & 0.009 \end{pmatrix}$	$\begin{pmatrix} 0.031 & 0.000 & 0.000 \\ 0.000 & 0.032 & 0.001 \\ 0.000 & 0.001 & 0.031 \end{pmatrix}$	$\begin{pmatrix} 0.472 & -0.001 & -0.001 \\ -0.001 & 0.468 & -0.002 \\ -0.001 & -0.002 & 0.471 \end{pmatrix}$
$\mathbf{K}_6$	$\begin{pmatrix} 0.007 & 0.000 & 0.000 \\ 0.000 & 0.007 & 0.000 \\ 0.000 & 0.000 & 0.007 \end{pmatrix}$	$\begin{pmatrix} 0.028 & 0.001 & 0.000 \\ 0.001 & 0.027 & 0.001 \\ 0.000 & 0.001 & 0.027 \end{pmatrix}$	$\begin{pmatrix} 0.356 & -0.003 & 0.000 \\ -0.003 & 0.359 & -0.003 \\ 0.000 & -0.003 & 0.357 \end{pmatrix}$
$\mathbf{K}_7$	$\begin{pmatrix} 0.007 & 0.000 & 0.000 \\ 0.000 & 0.007 & 0.000 \\ 0.000 & 0.000 & 0.007 \end{pmatrix}$	$\begin{pmatrix} 0.028 & -0.001 & 0.000 \\ -0.001 & 0.027 & -0.001 \\ 0.000 & -0.001 & 0.027 \end{pmatrix}$	$\begin{pmatrix} 0.356 & 0.003 & 0.000 \\ 0.003 & 0.359 & 0.003 \\ 0.000 & 0.003 & 0.357 \end{pmatrix}$
$\mathbf{K}_8$	$\begin{pmatrix} 0.018 & 0.000 & 0.000 \\ 0.000 & 0.018 & 0.000 \\ 0.000 & 0.000 & 0.018 \end{pmatrix}$	$\begin{pmatrix} 0.054 & 0.000 & -0.001 \\ 0.000 & 0.057 & -0.002 \\ -0.001 & -0.002 & 0.054 \end{pmatrix}$	$\begin{pmatrix} 0.455 & 0.003 & 0.002 \\ 0.003 & 0.459 & 0.002 \\ 0.002 & 0.002 & 0.457 \end{pmatrix}$

least square method. We note that for some of 22 ordering patterns depicted in Figure S1 the total energy was not employed as itself in the fitting procedure: For the ordering patterns in Figures S1e, j, and o, the difference between the total energies of the two ordering patterns was used; For the ordering patterns in Figure S1p, a specific combination of pluses and minuses of the total energies of the four ordering patterns was used as this particular choice gives the difference between $\mathbf{J}_3^{(1)}$ and $\mathbf{J}_3^{(2,3)}$. The spin directions of the transition metal ions were constrained to be along the collinear directions during the total energy calculations. In the case of $MnPS_3$ and $NiPS_3$, the collinear direction $\mathbf{n}$ was chosen to be $[1, 0, 0]^\mathsf{T}$, $[0, 1, 0]^\mathsf{T}$, $[0, 0, 1]^\mathsf{T}$, $[\sin\theta, 0, \cos\theta]^\mathsf{T}$, $[0, \sin\theta, \cos\theta]^\mathsf{T}$, and $[\cos\phi, \sin\phi, 0]^\mathsf{T}$ (in Cartesian coordinates), where $\theta = 30°$ and $\phi = 30°$. In the case of $FePS_3$, a different choice for $\mathbf{n}$ was made to more accurately capture the magnetic anisotropy that strongly favors the z direction: $\mathbf{n} = [\sin\theta_1, 0, \cos\theta_1]^\mathsf{T}$, $[0, \sin\theta_1, \cos\theta_1]^\mathsf{T}$, $[0, 0, 1]^\mathsf{T}$, $[\sin\theta_2, 0, \cos\theta_2]^\mathsf{T}$, $[0, \sin\theta_2, \cos\theta_2]^\mathsf{T}$, and $[\sin\theta_2 \cos\phi, \sin\theta_2 \sin\phi, \cos\theta_2]^\mathsf{T}$, where $\theta_1 = 30°$, $\theta_2 = 60°$, and $\phi = 30°$.

The standard deviations of the residual error (the difference between the actual first-principles value and the value obtained from our magnetic model) in the total energy per transition metal ion are $0.02\,\mu eV$, $16\,\mu eV$, and $0.2\,\mu eV$ for $MnPS_3$, $FePS_3$, and $NiPS_3$, respectively. For all $TMPS_3$'s, the errors were much smaller than their characteristic magnetic interaction parameters: (i) for $MnPS_3$ and $NiPS_3$, the residual error is simply negligible, and (ii) for $FePS_3$, it is two or three orders of magnitude smaller than λ, $\mathbf{J}_1^{(a)}$, and $\mathbf{J}_3^{(a)}$, which mostly determine the magnetic ordering, the critical temperature, and the Ising-like critical behavior of $FePS_3$, and also importantly the magnetic model for $FePS_3$ correctly predicted the magnetic ordering pattern of Figure S1g to be the lowest-energy configuration.

1.3 Constrained DFT+U calculations

We carried out DFT+U calculations using *our custom version* of Quantum ESPRESSO suite,[S4] in which we implemented a scheme that constrains the spin directions as proposed in ref S5 with our adaptations for the DFT+U method. In our implementation, the local (spin) magnetic moment at

the i-th magnetic atom $\mathbf{m}_i$ was chosen to be

$$\mathbf{m}_i = \sum_{s_1 s_2} \sum_m \sum_{n\mathbf{k}} \left\langle \psi_{n\mathbf{k}}^{s_1} \middle| \phi_{im} \right\rangle \sigma_{s_1 s_2} \left\langle \phi_{im} \middle| \psi_{n\mathbf{k}}^{s_2} \right\rangle, \tag{S4}$$

where s_1 and s_2 are the spinor indices, $\left| \psi_{n\mathbf{k}}^{s} \right\rangle$ is the spin s component of the Kohn-Sham spinor wavefunction with the band index n and momentum $\mathbf{k}$, $|\phi_{im}\rangle$ is the $3d$ atomic orbital of the i-th magnetic atom with the orbital magnetic quantum number m, and $\sigma_{s_1 s_2}$ is the (s_1, s_2) component of the Pauli matrices $\boldsymbol{\sigma} = (\sigma^x, \sigma^y, \sigma^z)$. Then the spin direction of the magnetic atom is constrained along a predefined direction $\mathbf{e}_i$ by minimizing the DFT total energy plus the penalty energy given as[S5]

$$E_p = \sum_i \Lambda_i \left(|\mathbf{m}_i| - \mathbf{e}_i \cdot \mathbf{m}_i \right), \tag{S5}$$

where Λ_i determines how close the constrained spin direction of $\mathbf{m}_i$ will be to $\mathbf{e}_i$. In our calculations Λ_i was typically set to 1 Ry, which yielded well-converged local magnetic moments, $\mathbf{m}_i$'s, close to their target directions, $\mathbf{e}_i$'s.

Since only the directions of the magnetic moments are constrained, their magnitudes can in principle be different from configuration to configuration. However, the standard deviation of the magnitude of the local magnetic moments over all the configurations shown in Figure S1 turned out to be very small, being only 0.13 %, 0.28 %, and 3.6 % of the corresponding average magnitudes for $MnPS_3$, $FePS_3$, and $NiPS_3$, respectively.

1.4 Further computational details

The exchange-correlation functional within the local density approximation (LDA) parametrized by Perdew and Zunger[S6] was used to calculate the exchange-correlation energy. We employed a rotationally invariant LDA+U method suggested by Liechtenstein $et\,al.$[S7] The effective Coulomb interaction U was set to 6.5 eV and 4 eV for $NiPS_3$ and the other $TMPS_3$'s, respectively. In determining the U values, we first tested several different U values in the range 3–7 eV and chose the values that provide reasonable estimates for the T_N of the bulk $TMPS_3$ compounds. We then carried

out linear response calculations with the hp.x program[S8] in the Quantum ESPRESSO suite to see whether those empirical U values could be supported by the well-established framework for computing U values from first principles. Our linear response calculations yielded 2.9 eV, 3.9 eV, and 6.6 eV for the transition metal elements for bulk $MnPS_3$, $FePS_3$, and $NiPS_3$, respectively, which are in good agreement with our empirically chosen U values. We also checked that the similarly calculated U values in the cases of monolayer $MnPS_3$, $FePS_3$, and $NiPS_3$ were very similar to the corresponding bulk values (the differences were less than 0.01 eV). In general, U tends to increase across the row in the periodic table (from left to right) as the $3d$ electrons get more localized.[S9] In terms of U, therefore, $CoPS_3$ (Z=27 for Co) is expected to be somewhere between $FePS_3$ (Z=26 for Fe) and $NiPS_3$ (Z=28 for Ni); that would explain the gap between the U of $FePS_3$ and that of $NiPS_3$.

Optimized, norm-conserving pseudopotentials[S10,S11] that include the relativistic effects were used to simulate the interactions between the nuclei and electrons. The kinetic energy cutoff of the plane-wave basis was set to 80 Ry.

The atomic coordinates of a bilayer $TMPS_3$ were adopted from the atomic coordinates of the bulk structure reported from an experimental study;[S12] to avoid spurious interactions between periodic images, a vacuum layer with 18 Å thickness was placed between the adjacent periodic images. Because of the over-binding behavior of the LDA, we did not carry out further structural relaxations. This over-binding behavior of the LDA has always been a notorious problem because a physical property of a material is often sensitive to its geometry. And when the LDA fails to provide a reasonable result for the structure, as it really does in the case of $TMPS_3$ as well as in the cases of many other materials, there is no way but to resort to the experimental structure since a structural relaxation with the LDA plus a van der Waals correction is not a viable option since all the available van der Waals correction methods are designed to work with the GGA. (In Section 1.5 of this Supporting Information, we show why we chose to use the LDA and not the GGA.) Fortunately, keeping the experimental structure is known to give good results for the magnetic properties,[S13–S18] which are the main focus of our study, and we therefore used the experimental

structure.

In addition, when we performed structural relaxations for monolayer and bulk $NiPS_3$ (within the LDA using scalar-relativistic pseudopotentials), all the in-plane lattice parameters and the distances between Ni–Ni, Ni–S, P–P, and P–S within an $NiPS_3$ layer were essentially the same, being different by at most 0.15 %, supporting the use of the bulk structures for the few-layer cases.

We also note that the effects of strain on the previous Raman study of $NiPS_3$[S19] was small because (i) the samples were made by exfoliation, and not by epitaxial growth, and (ii) experiments on two different substrates (SiO_2 and hexagonal boron nitride) resulted in almost the same Raman spectra.

We calculated the total energy for a supercell (Figure S1) having $N_1 \times N_2 \times 1$ unit cells of nonmagnetic $TMPS_3$ (Figure S2), where (N_1, N_2) is (1, 1), (2, 1), (1, 2), (4, 1), and (1, 4). To keep the k-point density in the reciprocal space for the calculations involving supercells of different size the same, we used an $8/N_1 \times 8/N_2 \times 1$ Monkhorst-Pack grid[S20] in the case of the $N_1 \times N_2 \times 1$-supercell calculations.

1.5   Note on exchange-correlation functional with non-collinear magnetism

In this work, we did not use the generalized gradient approximation (GGA) because the GGA with noncollinear magnetism (GGA+NCM) causes severe numerical instabilities (note that we need NCM thanks to spin-orbit coupling); with the GGA+NCM, we were not able to reach the level of accuracy needed to resolve the magnetic anisotropy energy, which could be as small as a few tens of μeV per transition metal atom. The GGA+NCM, of which a widely adopted formulation was proposed in ref S21, has "both formal and numerical problems".[S22] The computational issue most likely emerges from small regions in space where spin density is close to zero. Here, if the local spin polarization changes slowly in space passing through zero, its direction is reverted. This reversal in the direction of the local spin polarization is not a big deal in reality because the magnitude of the local spin polarization is zero. One remarkable peculiarity of the GGA+NCM is that even if the spin density changes smoothly over such regions, the GGA+NCM functional

recognizes it as a kink, the gradient of which is singular, thus causing severe numerical instabilities.

We examined how this serious issue had been dealt with in some public software packages. Surprisingly, currently there is no systematic solution for these instabilities based on justifiable theory but only ad hoc methods have been made without sound theoretical justification. In the case of the Elk code,[S23] for example, the kinks were smoothed out by preventing the magnitude of magnetization density from being smaller than a threshold. We would have applied this prescription to our code if it had been possible to keep this threshold sufficiently small while attaining a reasonable degree of convergence. We found, however, that the threshold had to be fairly large for convergence, so that it would affect the small magnetic anisotropies that we wanted to determine as accurately as possible. In the case of VASP,[S24] this inherent instability of GGA+NCM can be dealt with by using its own variation (whose formal and conceptual validity is not discussed) different from the original formulation of ref S21. In passing we note that Quantum ESPRESSO did not make such ad hoc, unjustifiable compromises and hence it transparently shows the serious instability problem inherent in the GGA+NCM.

In fact, the numerical instability of the GGA+NCM is deeply related with its formal problem, as the scheme completely ignores the contribution to the exchange-correlation energy due to the gradient of magnetization density perpendicular to the local magnetization direction, while the exact exchange-correlation energy is certainly affected by that contribution.[S25] There have been a few papers addressing this issue and proposing different formulations of the GGA+NCM,[S22,S26] but none of them really complied with the conditions that should be satisfied by the exact exchange-correlation energy; by the way, one of them has been retracted.[S27] In contrast, the LDA is free from such issues. Therefore, we decided to use the LDA instead of the GGA to meet our strict criterion for convergence and to avoid the risk of being affected by those inherent problems of the GGA+NCM scheme.
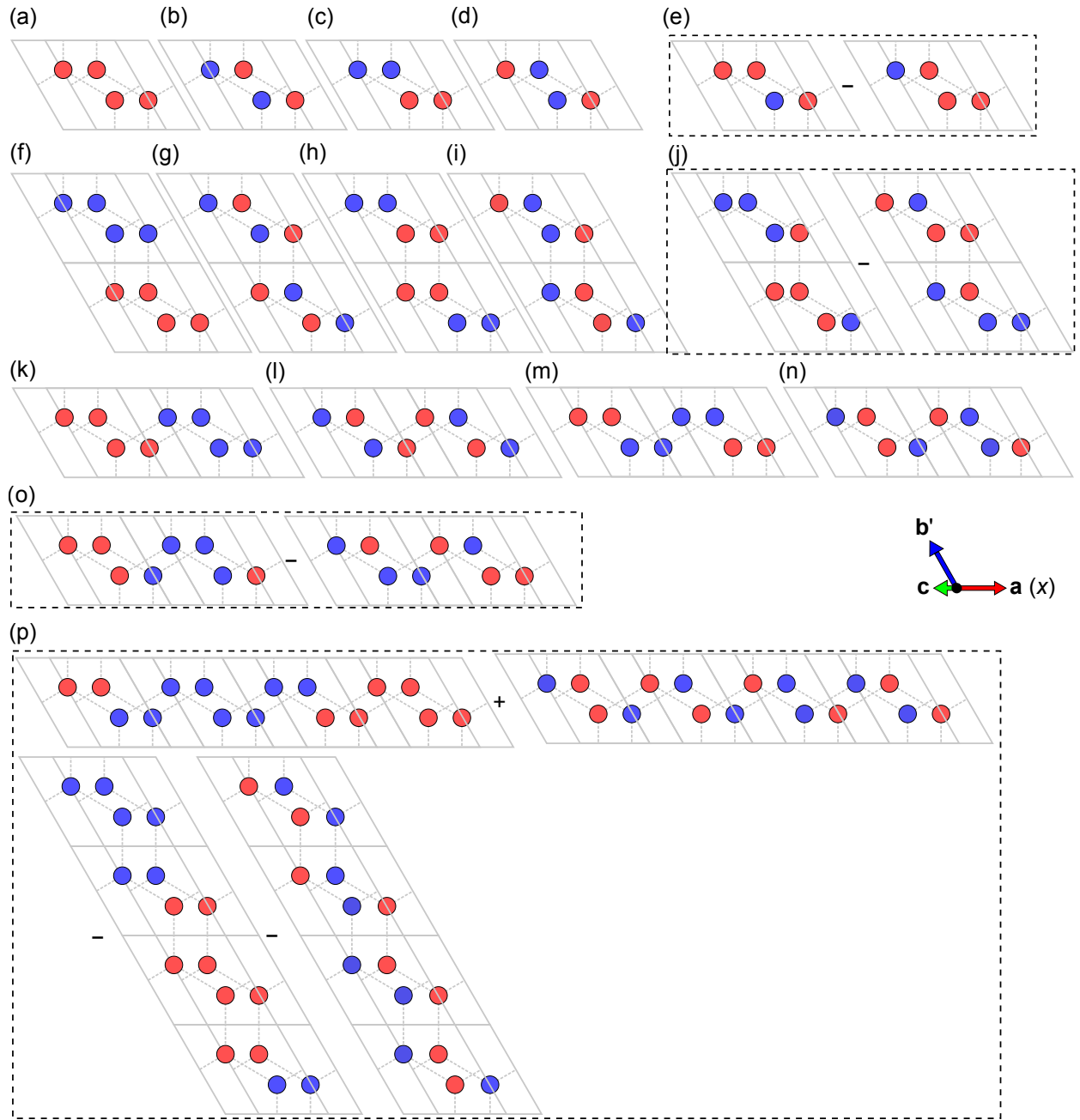
Figure S1: Top view of the collinear magnetic patterns of bilayer TMPS$_3$ used to calculate the parameters of the anisotropic magnetic model (eq S1). The red and blue disks represent the spin-up and spin-down transition metal ions, respectively, with respect to the collinear direction.
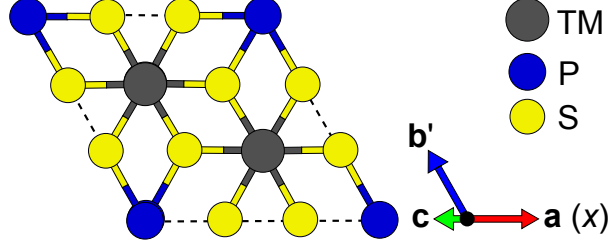
Figure S2: Top view of the primitive unit cell of nonmagnetic TMPS$_3$.

2   Calculation details: dipolar anisotropy

The contribution of the magnetic dipole-dipole interactions between localized magnetic moments to our magnetic model is given by the usual expression:

$$H_{\text{dip}} = \frac{1}{2} \sum_{i=1}^{N} \sum_{j=1,j\neq i}^{N} \left[\frac{\mathbf{m}_i \cdot \mathbf{m}_j}{r_{ij}^3} - \frac{3(\mathbf{m}_i \cdot \mathbf{r}_{ij})(\mathbf{m}_j \cdot \mathbf{r}_{ij})}{r_{ij}^5} \right]. \tag{S6}$$

The paramagnetic susceptibilities of MnPS$_3$ and NiPS$_3$ are well described by the spin-only magnetic moments of S = 2.5 and S = 1, respectively.[S28] This indicates that $\mathbf{m}_i$ for MnPS$_3$ and NiPS$_3$ is given by $2\mu_{\text{B}}\mathbf{S}_i$, where μ_{B} is the Bohr magneton. In the case of FePS$_3$ (S = 2), on the other hand, $\mathbf{m}_i$ is also contributed by the orbital polarizations. The z component of $\mathbf{m}_i$ is now given by $m_{iz} = \mu_{\text{B}}(2S_{iz} + L_{iz})$, while the x and y components have no orbital contributions and are given by $m_{ix} = 2\mu_{\text{B}}S_{ix}$ and $m_{iy} = 2\mu_{\text{B}}S_{iy}$, respectively. Because H_{dip} is negligibly small compared to the magnetic anisotropy arising from LS coupling and a nonzero L_{iz} (= ± 1) affects only a fraction (~25%) of m_{iz}, whether the orbital contributions (the terms that include L_{iz}) of H_{dip} are exactly treated or not is of no importance at all in discussing the magnetic ordering of FePS$_3$. In our calculations, H_{dip} for FePS$_3$ was evaluated with $\mathbf{m}_i = 2\mu_{\text{B}}\mathbf{S}_i$ so that the spin-only part of H_{dip} was taken into account, but this term can also be dropped in investigating the magnetic ordering in FePS$_3$ (see the negligible difference between Figures 2e and h of the main manuscript).

   Here, we further look into the effects of the dipolar anisotropy on the magnetic anisotropy of TMPS$_3$ by calculating H_{dip} for the ground-state magnetic configurations of bulk TMPS$_3$ (the

configurations shown in Figures S1c, g, and f for $MnPS_3$, $FePS_3$, and $NiPS_3$, or, equivalently, in Figures 2a–c in the main manuscript, respectively) and examining the differences between the values of H_{dip} evaluated with imposing different collinear spin directions (x, y, and z) for $\mathbf{m}_i$'s. We circumvented the issue of dealing with summing over infinitely many pairs of the magnetic sites (i and j in eq S6) by neglecting the terms of which the distance between the spins r_{ij} is longer than a certain cutoff r_{cut}. The convergence of the dipolar anisotropy with respect to the cutoff distance was tested for several values of r_{cut} ranging from 5 Å to 50 Å.

As Figure S3 shows, the choice of $r_{cut} = 9$ Å yields reasonably converged results for the dipolar anisotropy of $TMPS_3$ (see the vertical dotted lines). In the case of $MnPS_3$ (Figure S3a), H_{dip} favors an easy-axis anisotropy along z. In the case of $FePS_3$ and $NiPS_3$ (Figures S3b and c), it gives rise to easy-axis anisotropies along the x direction. The magnitude of the dipolar anisotropy is about a few tens of μeV, ranging between 10 μeV and 80 μeV, per transition metal ion.
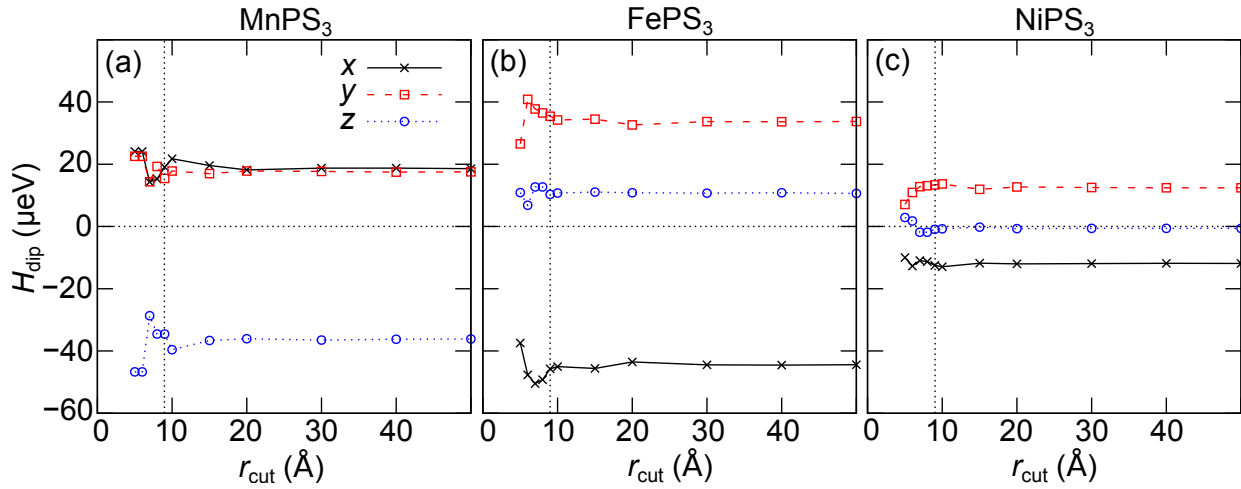

Figure S3: Convergence of the dipolar anisotropy, H_{dip} (eq S6) per transition metal ion, with respect to the cutoff distance r_{cut}. The vertical dotted lines are placed at $r_{cut} = 9$ Å.

3 Effects of *LS* coupling on the magnetic anisotropy energy and some related numerical issues

3.1 Effects of *LS* coupling in FePS$_3$

Given that *LS* coupling dominantly contributes to the magnetic anisotropy of FePS$_3$, its (effective) functional form with respect to the orbital and spin polarizations can be assessed by looking at how the orbital polarization of an Fe ion and the total energy of the system change with the direction of the spin polarization. Here, we present a simple analysis based on our DFT+U calculations using fully-relativistic pseudopotentials that can justify the specific form of the *LS* coupling term, $\sum_{i=1}^{N} \lambda L_{iz} S_{iz}$, used in our magnetic model (eq S1).

We calculated the total energy of bilayer FePS$_3$ and the orbital polarization of an Fe ion within the system for ferromagnetic configurations (Figure S1a) of various collinear spin directions. The choice of using the ferromagnetic ordering is just for convenience, because then all the transition metal ions have the same orbital and spin polarizations ($L_z = L_{iz}$ and $S_z = S_{iz}$ for all i). We have checked that the results are essentially the same if we use the ground state magnetic configuration (Figure S1g).

Figure S4a shows the orbital polarization of an Fe ion as a function of the direction of its spin polarization. The z component of the orbital polarization is unquenched and is almost constant ($L_z \sim 1$) as the spin rotates fully (by 360° in the yz plane as depicted) while the other components remain relatively small. Figure S4b displays the effect of this unquenched L_z on the magnetic anisotropy. It shows the total energy of the magnetic configurations with $L_z \approx 1$ and $L_z \approx -1$. At $\theta = 90°$, where the spin lies in the xy plane, there is a cusp in the lowest-energy curve (the dash-dotted blue curve in Figure S4b), which is a direct consequence of the two-fold degeneracy arising from the orbital degrees of freedom (L_z being either 1 or -1). This $|\cos\theta|$ dependence on the collinear spin direction is differentiated from the usual $\cos^2\theta$ dependence of the contributions arising from the other terms in eq S1. A similar analysis was done for the ground-state magnetic

configuration (Figure S1h or, equivalently, Figure 2b in the main manuscript) and the same $|\cos\theta|$ dependence was obtained.

We note that a delicate handling of the initial occupation matrix was required especially when we tried to calculate the total energy for the magnetic configurations whose local spins were aligned with the hard axes, the x and y directions. And this numerical issue is closely related to the two-fold degeneracy shown at $\theta = 90°$ and $270°$ in Figure S4b. We had to initialize the occupation matrix with complex numbers so that the initial occupation matrix had unquenched orbital angular momentum (e.g. $L_z = \pm1$), and only through that way the correct, orbital-polarized ground states were obtained. Since filling the initial occupation matrix with complex numbers is not the common practice for LDA+U calculations, it is likely that even experts in first-principles calculations might have missed this delicate total energy minimum.

3.2 Failure of magnetic force theorem

The influence of orbital degrees of freedom is not restricted to the sensitiveness to the initial condition on the occupation matrix. What is more important is that it excludes the use of the magnetic force theorem (MFT)[S29] from consideration. Since knowing how the MFT is working is important to understand why it should not be used in the case of FePS$_3$, we will shortly describe how the method is commonly implemented. First, a non-relativistic, self-consistent calculation is carried out to obtain well-converged collinear spin densities (two scalar quantities for up and down channels). Thus obtained spin densities have no preference for a specific direction, as they are only representing a collinear spin system. They are converted to a magnetization density (a vector quantity), and its collinear direction is then rotated toward a certain direction, usually the x, y or z direction. The rotated vector quantity is then used to initiate a fully-relativistic, non-self-consistent calculation. Such a one-shot calculation is repeated for other directions. Finally, the magnetic anisotropy energy is calculated from comparing the sum of the (Kohn-Sham) energy eigenvalues resulted from one of such non-self-consistent calculations with those for other directions.

The advantage of the MFT method is immediately noticed: because the method treats spin-orbit

coupling as a perturbation, it circumvents all the intricacies that would be faced if a self-consistency with including the effects of spin-orbit coupling were to be achieved. The disadvantage by contrast is not that obvious. An important note here is that a non-relativistic calculation always yields spin densities without orbital degrees of freedom. (Note that the contribution to the orbital polarization of a Bloch state $\psi_{n\mathbf{k}}$ is cancelled by its complex conjugate—which is a symmetry operation of the Hamiltonian if spin-orbit coupling is absent—state with Bloch wavevector $-\mathbf{k}$.) While the MFT assumes implicitly that spin-orbit coupling is a small perturbation, the effects of spin-orbit coupling are significant in $FePS_3$, as they result in orbital polarizations, which are forbidden in non-relativistic treatments. The basic assumption of the MFT is thus no longer satisfied. In other words, the magnetic anisotropy of $FePS_3$ should not be handled with the MFT.

However, recent theoretical studies on $FePS_3$ adopted the MFT and consequently reported much smaller (by almost two orders of magnitude) values for the magnetic anisotropy,[S30,S31] explaining why we had to resort to the computationally much trickier and heavier brute-force, total-energy method. Both our own MFT calculations on $FePS_3$ and more involved total energy calculations without using a good (i.e., filled with properly designed complex elements) initial occupation matrix resulted in metastable states whose energy was quantitatively very similar to those reported in these two papers.[S30,S31]

4   Additional comments on calculated exchange interactions

4.1   Possible influence of the exchange-correlation functional on the intra-lyer exchange interactions and the Néel temperature of $NiPS_3$

We suspect that a possible reason for the discrepancy in bulk T_N between our calculation results (192 K, see Figures 2f and o in the main manuscript) and experiments (155 K[S3,S28]) in the case of $NiPS_3$ could be the use of the LDA. In our test calculations using scalar-relativistic pseudopotentials, the use of the GGA for the exchange-correlation energy[S32] yielded smaller values for $J_3^{(1-3)}$, which in turn could decrease the estimated T_N for bulk $NiPS_3$. We also note that the estimates of
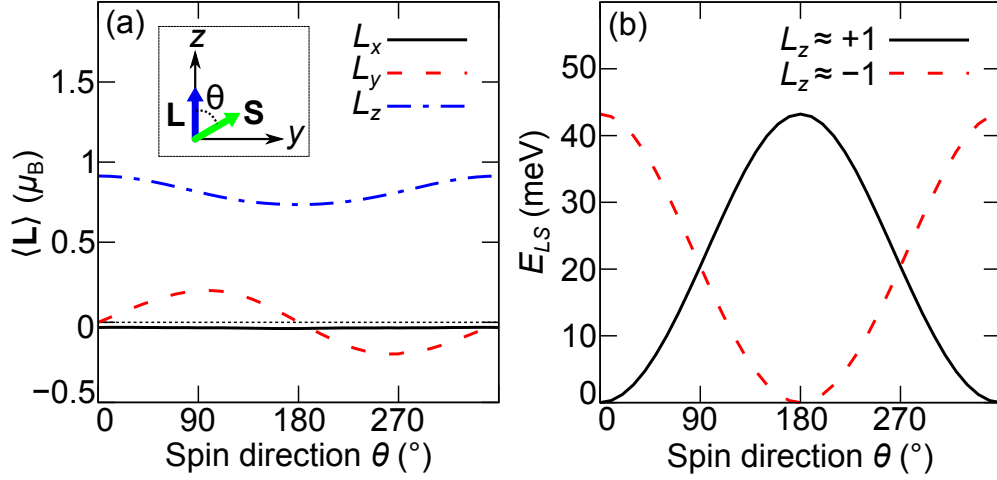
Figure S4: (a) Orbital polarization of an Fe ion in $FePS_3$ as a function of the direction of its spin polarization. Here, θ is the angle from z (the out-of-plane direction of an $FePS_3$ monolayer) of the spin polairzation direction. (b) Magnetic anisotropy energy per Fe ion as a function of the spin polarization direction. The solid black curve and the dashed red curve represent the case of an Fe ion with $L_z \approx 1$ and that of an Fe ion with $L_z \approx -1$, respectively. The dash-dotted blue curve, which is slightly shifted downward for visual clarity, shows the lowest-energy at a given spin polarization direction.

$J_3^{(1-3)}$ from other first-principles studies [S31,S33] using the GGA tended to be smaller than those from our LDA calculations. However, the GGA is not an option for the assessment of the magnetic anisotropy of $TMPS_3$'s because of the severe numerical instability inherent in the formulation of the GGA with noncollinear magnetism; see Section 1.5 for our detailed comments on the numerical and formal aspects of this issue.

4.2 Unexpectedly large interlayer exchange interactions in $NiPS_3$

Table S4 shows the isotropic interlayer exchange interaction K_n (= $1/3\,\mathrm{Tr}\,\mathbf{K}_n$) obtained from our calculations. For all $TMPS_3$'s the second-nearest-neighbor isotropic interlayer exchange interactions ($K_{3,4}$) are relatively large compared to the other K_n's. Particularly in the case of $NiPS_3$, $K_{3,4}$ are 1.64 meV and as large as 30 % of $J_1^{(1-3)}$, indicating strong influence of the thickness on the magnetic properties of this compound. It is noteworthy that superexchange paths for K_n's need to go through at least two S ions, e. g., like TM-S-S-TM, and that such pathways are similar in

their total length for all K_n's considered in this work. This similarity partly explains how $K_{3,4}$ can be comparable to or even larger than the nearest-neighbor interlayer exchange interactions ($K_{1,2}$). Further investigation on the exchange mechanism behind K_n's, which is beyond the scope of our paper, would be helpful to address this issue, and we leave it for future studies.

Table S4: Isotropic interlayer exchange interaction K_n in units of meV.

	K_1	K_2	K_3	K_4	K_5	K_6	K_7	K_8
MnPS$_3$	0.01	0.01	0.03	0.03	0.01	0.01	0.01	0.02
FePS$_3$	0.04	0.04	0.11	0.12	0.03	0.03	0.03	0.05
NiPS$_3$	−0.05	−0.08	1.64	1.64	0.47	0.36	0.36	0.46

5   Calculations details: classical Monte Carlo simulation

In our classical Monte Carlo simulations, the Metropolis algorithm[S34] and a variant of the Wolff cluster algorithm,[S35] modified for inclusion of the anisotropic exchange interactions[S36] and the single-ion anisotropy,[S37] were used to update spins during simulations. For each measurement, one Metropolis sweep of the entire spin lattice and 10 Wolff cluster updates were done. Typically, 10^4–10^5 measurements were done for calculating thermodynamic quantities at a given temperature. The initial 20–50% of those measurements were discarded for thermalization. In the case of bulk TMPS$_3$, periodic boundary conditions were imposed for all the crystallographic directions (**a**, **b′**, and **c** in Figure S2). We found that a superlattice containing $128 \times 128 \times 8$ unit cells including $128 \times 128 \times 8 \times 2 = 4096$ spins was sufficient to converge the results. In the case of few-layer TMPS$_3$, periodic boundary conditions were used for only the in-plane directions (**a** and **b′** in Figure S2). A $128 \times 128 \times 1$ superlattice was employed for the few-layer cases.

The magnetic susceptibility χ_μ and the specific heat arising from the localized magnetic moments c_v^{mag} are defined as

$$\chi_\mu = \frac{\langle M_\mu^2 \rangle - \langle M_\mu \rangle^2}{NT} \tag{S7}$$

and

$$c_v^{\mathrm{mag}} = \frac{\langle H_{\mathrm{tot}}^2 \rangle - \langle H_{\mathrm{tot}} \rangle^2}{NT^2}, \tag{S8}$$

respectively, where μ denotes the Cartesian direction x, y, and z, N is the number of magnetic atoms, T is the temperature, and M_μ is the total magnetic moment. The expression $\langle O \rangle$ denotes the thermal average of a quantity O, i.e. the average of O with the Boltzmann weight factor. In the case of MnPS$_3$ and NiPS$_3$, where the orbital degrees of freedom are suppressed ($L_{iz} = 0$) by the crystal field effects, $\langle O \rangle$ is simply a weighted average of $O[\{\mathbf{S}_i\}]$ over all spin configuration $\{\mathbf{S}_i\}$'s. It is straightforward to calculate this kind of weighted averages by using the importance sampling method, which is inherent in the process of updating spins by the algorithms we employed. If additional degrees of freedom arising from the orbital polarization should be considered, as in the case of FePS$_3$, things become much more complicated because then $\langle O \rangle$ involves averaging over all possible orbital configurations, $\{L_{iz}\}$'s, as well as $\{\mathbf{S}_i\}$'s. In Section 6, we discuss how to resolve this issue in practice.

6 Orbital contributions to the magnetic susceptibility and specific heat

We present a detailed description of how the effects of the orbital degrees of freedom on thermodynamic quantities were treated in our Monte Carlo simulations. The basic idea is to integrate out orbital degrees of freedom in advance of averaging over spin degrees of freedom. We first consider the partition function Z of the anisotropic magnetic model H_{tot} (eq S1):

$$Z = \sum_{\{\mathbf{S}_i\}} \sum_{\{L_{iz}\}} \left\{ \exp\left[-\beta \left(H_{S\,\mathrm{only}} + \sum_{i=1}^{N} \lambda L_{iz} S_{iz} \right) \right] \right\}, \tag{S9}$$

where β is the inverse temperature $(k_B T)^{-1}$ and $H_{S\,\text{only}}$ is the spin-only-dependent part of H_{tot} which reads

$$H_{S\,\text{only}} = \frac{1}{2} \sum_{i=1}^{N} \sum_{n=1}^{3} \sum_{a=1}^{M_n} \mathbf{S}_i^{\mathsf{T}} \mathbf{J}_n^{(a)} \mathbf{S}_{j(i,\mathbf{J}_n^{(a)})} + \frac{1}{2} \sum_{i=1}^{N} \sum_{n=1}^{8} \mathbf{S}_i^{\mathsf{T}} \mathbf{K}_n \mathbf{S}_{j(i,\mathbf{K}_n)}$$
$$+ \sum_{i=1}^{N} \mathbf{S}_i^{\mathsf{T}} \mathbf{D} \mathbf{S}_i + H_{\text{dip}}. \tag{S10}$$

The summation over $\{L_{iz}\}$ in eq S9 can be done readily by exploiting that L_{iz} can be either 1 or -1:

$$Z = \sum_{\{\mathbf{S}_i\}} \left\{ \exp(-\beta H_{S\,\text{only}}) \sum_{\{L_{iz}\}} \left[\prod_{i=1}^{N} \exp\left(-\beta \lambda L_{iz} S_{iz}\right) \right] \right\}$$
$$= \sum_{\{\mathbf{S}_i\}} \left\{ \exp(-\beta H_{S\,\text{only}}) \prod_{i=1}^{N} \left[\sum_{L_{iz}=\pm 1} \exp\left(-\beta \lambda L_{iz} S_{iz}\right) \right] \right\}$$
$$= \sum_{\{\mathbf{S}_i\}} \left\{ \exp(-\beta H_{S\,\text{only}}) \prod_{i=1}^{N} 2 \cosh\left(-\beta \lambda S_{iz}\right) \right\}$$
$$= \sum_{\{\mathbf{S}_i\}} \left\{ \exp\left[-\beta \left(H_{S\,\text{only}} + \sum_{i=1}^{N} V_i(\beta, \lambda) \right) \right] \right\}, \tag{S11}$$

where $V_i(\beta, \lambda) = -\beta^{-1} \ln\left[2 \cosh\left(-\beta \lambda S_{iz}\right) \right]$. Here, $V_i(\beta, \lambda)$ can be thought of as an effective on-site potential that accounts for the effects of orbital degrees of freedom at a given temperature T.

The z component of the total magnetic moment $\langle M_z \rangle = \mu_B \langle L_z + 2S_z \rangle$, where $L_z = \sum_{i=1}^{N} L_{iz}$ and

$S_z = \sum_{i=1}^{N} S_{iz}$. The spin part can be written as

$$
\begin{aligned}
\langle S_z \rangle &= Z^{-1} \sum_{\{\mathbf{S}_i\}} \sum_{\{L_{iz}\}} \left\{ S_z \exp\left[-\beta\left(H_{S\,\text{only}} + \sum_{i=1}^{N} \lambda L_{iz} S_{iz} \right) \right] \right\} \\
&= Z^{-1} \sum_{\{\mathbf{S}_i\}} \left\{ S_z \exp(-\beta H_{S\,\text{only}}) \sum_{\{L_{iz}\}} \left[\prod_{i=1}^{N} \exp\left(-\beta\lambda L_{iz} S_{iz} \right) \right] \right\} \\
&= Z^{-1} \sum_{\{\mathbf{S}_i\}} \left[S_z \exp(-\beta H_{S\,\text{only}}) \prod_{i=1}^{N} 2\cosh\left(-\beta\lambda S_{iz} \right) \right] \\
&= Z^{-1} \sum_{\{\mathbf{S}_i\}} \left\{ S_z \exp\left[-\beta\left(H_{S\,\text{only}} + \sum_{i=1}^{N} V_i(\beta, \lambda) \right) \right] \right\} \\
&= \langle S_z \rangle_S \,.
\end{aligned}
\tag{S12}
$$

Here, the notation $\langle O \rangle_S$ was used to emphasize that the average was taken over spin configuration $\{\mathbf{S}_i\}$'s only, with the weight factor $Z^{-1} \exp[-\beta(H_{S\,\text{only}} + \sum_{i=1}^{N} V_i(\beta, \lambda))]$. The orbital part can be written

as a sum over possible spin configurations as well, i.e.

$$
\begin{aligned}
\langle L_z \rangle &= Z^{-1} \sum_{\{S_i\}} \sum_{\{L_{iz}\}} \left\{ L_z \exp\left[-\beta\left(H_{S\,\text{only}} + \sum_{i=1}^{N} \lambda L_{iz} S_{iz} \right) \right] \right\} \\
&= Z^{-1} \sum_{\{S_i\}} \left\{ \exp(-\beta H_{S\,\text{only}}) \sum_{\{L_{iz}\}} \left[L_z \prod_{i=1}^{N} \exp(-\beta\lambda L_{iz} S_{iz}) \right] \right\} \\
&= Z^{-1} \sum_{\{S_i\}} \left\{ \exp(-\beta H_{S\,\text{only}}) \sum_{\{L_{iz}\}} \left[\sum_{j=1}^{N} L_{jz} \prod_{i=1}^{N} \exp(-\beta\lambda L_{iz} S_{iz}) \right] \right\} \\
&= Z^{-1} \sum_{\{S_i\}} \left\{ \exp(-\beta H_{S\,\text{only}}) \sum_{j=1}^{N} \left[2\sinh(-\beta\lambda S_{jz}) \prod_{i=1,i\neq j}^{N} 2\cosh(-\beta\lambda S_{iz}) \right] \right\} \\
&= Z^{-1} \sum_{\{S_i\}} \left\{ \exp(-\beta H_{S\,\text{only}}) \sum_{j=1}^{N} \left[l_{jz} \prod_{i=1}^{N} 2\cosh(-\beta\lambda S_{iz}) \right] \right\} \\
&= Z^{-1} \sum_{\{S_i\}} \left\{ \left(\sum_{j=1}^{N} l_{jz} \right) \exp\left[-\beta\left(H_{S\,\text{only}} + \sum_{i=1}^{N} V_i(-\beta\lambda S_{iz}) \right) \right] \right\} \\
&= Z^{-1} \sum_{\{S_i\}} \left\{ l_z \exp\left[-\beta\left(H_{S\,\text{only}} + \sum_{i=1}^{N} V_i(\beta,\lambda) \right) \right] \right\} \\
&= \langle l_z \rangle_S ,
\end{aligned}
\tag{S13}
$$

where $l_{iz} = \tanh(-\beta\lambda S_{iz})$ and $l_z = \sum_{i=1}^{N} l_{iz}$.

Some higher-order moments, such as $\langle L_z^2 \rangle$, $\langle S_z L_z \rangle$, and $\langle S_z^2 L_z^2 \rangle$, which are needed in calculating

χ_z and c_v^{mag}, are written as

$$
\langle L_z^2 \rangle = Z^{-1} \sum_{\{\mathbf{S}_i\}} \sum_{\{L_{iz}\}} \left\{ L_z^2 \exp\left[-\beta\left(H_{S\,\text{only}} + \sum_{i=1}^{N} \lambda L_{iz} S_{iz} \right) \right] \right\}
$$

$$
= Z^{-1} \sum_{\{\mathbf{S}_i\}} \left\{ \exp(-\beta H_{S\,\text{only}}) \sum_{\{L_{iz}\}} \left[L_z^2 \prod_{i=1}^{N} \exp(-\beta\lambda L_{iz} S_{iz}) \right] \right\}
$$

$$
= Z^{-1} \sum_{\{\mathbf{S}_i\}} \left\{ \exp(-\beta H_{S\,\text{only}}) \sum_{\{L_{iz}\}} \left[\sum_{j=1}^{N} \sum_{k=1}^{N} L_{jz} L_{kz} \prod_{i=1}^{N} \exp(-\beta\lambda L_{iz} S_{iz}) \right] \right\}
$$

$$
= Z^{-1} \sum_{\{\mathbf{S}_i\}} \left\{ \exp(-\beta H_{S\,\text{only}}) \sum_{\{L_{iz}\}} \left[\sum_{j=1}^{N} \left(1 + \sum_{k=1,k\neq j}^{N} L_{jz} L_{kz} \right) \prod_{i=1}^{N} \exp(-\beta\lambda L_{iz} S_{iz}) \right] \right\}
$$

$$
= Z^{-1} \sum_{\{\mathbf{S}_i\}} \left\{ \exp(-\beta H_{S\,\text{only}}) \sum_{j=1}^{N} \left[\left(1 + \sum_{k=1,k\neq j}^{N} l_{jz} l_{kz} \right) \prod_{i=1}^{N} 2\cosh(-\beta\lambda S_{iz}) \right] \right\}
$$

$$
= Z^{-1} \sum_{\{\mathbf{S}_i\}} \left\{ \exp(-\beta H_{S\,\text{only}}) \sum_{j=1}^{N} \left[\left(1 - l_{jz}^2 + \sum_{k=1}^{N} l_{jz} l_{kz} \right) \prod_{i=1}^{N} 2\cosh(-\beta\lambda S_{iz}) \right] \right\}
$$

$$
= Z^{-1} \sum_{\{\mathbf{S}_i\}} \left\{ \left[l_z^2 + \sum_{j=1}^{N} (1 - l_{jz}^2) \right] \exp\left[-\beta(H_{S\,\text{only}} + \sum_{i=1}^{N} V_i(\beta,\lambda)) \right] \right\}
$$

$$
= \left\langle l_z^2 + \sum_{i=1}^{N} (1 - l_{iz}^2) \right\rangle_S , \tag{S14}
$$

$$
\langle S_z L_z \rangle = \langle S_z l_z \rangle_S , \tag{S15}
$$

and

$$
\langle S_z^2 L_z^2 \rangle = \left\langle S_z^2 \left\{ l_z^2 + \sum_{i=1}^{N} (1 - l_{iz}^2) \right\} \right\rangle_S , \tag{S16}
$$

respectively.

Putting eqs S12–S16 into eqs S7 and S8, we obtain the expressions for χ_z and c_v^{mat}:

$$
\chi_z = \mu_B^2 \frac{\langle (l_z + 2S_z)^2 \rangle_S - \langle l_z + 2S_z \rangle_S^2 + \langle \sum_{i=1}^{N} (1 - l_{iz}^2) \rangle_S}{NT}. \tag{S17}
$$

and

$$c_v^{\text{mag}} = \frac{\langle H_{\text{tot,eff}}^2 \rangle_S - \langle H_{\text{tot,eff}} \rangle_S^2 + \langle \lambda^2 \sum_{i=1}^{N}(1 - l_{iz}^2)S_{iz}^2 \rangle_S}{NT^2}, \tag{S18}$$

respectively, where $H_{\text{tot,eff}} = H_{S\,\text{only}} + \sum_{i=1}^{N} \lambda l_{iz} S_{iz}$.

7 Quantum fluctuation effects on the stability of the antiferromagnetic ground state of monolayer NiPS$_3$

The isotropic intralayer exchange interactions ($J_n^{(a)}$, up to 28 meV) are much larger in magnitude than other constituents of our magnetic Hamiltonian for NiPS$_3$: the anisotropic intralayer exchange interactions (the traceless part of $\mathbf{J}_n^{(a)}$, ~0.07 meV), the single-ion anisotropy ($\mathbf{D}$, ~0.1 meV), and the dipolar anisotropy energy (~0.025 meV per transition metal ion). Therefore, we consider the quantum fluctuation effects in the J_1-J_2-J_3 Heisenberg model to gain insight into the possibility of a quantum spin liquid phase in monolayer NiPS$_3$.

Because $S=1$ for the Ni^{2+} ions ($3d^8$, high-spin configuration), the quantum effects of $S=1$ are of our particular interest. According to a study on the quantum ($S=1/2$ and $S=1$) J_1-J_2-J_3 model on the honeycomb lattice,[S38] the quantum spin liquid phase, which exists in a very small region in the parameter space in the case of $S=1/2$ (by the way, the sets of parameters for all three TMPS$_3$ compounds are outside this small region), disappears in the case of $S=1$ due to the weakening of quantum fluctuations. A spin liquid phase driven by the frustration arising from competing J_1, J_2, and J_3 is therefore not likely to happen.

In addition to the suppression of the quantum spin liquid phase, the phase boundaries of the classical J_1-J_2-J_3 model on the honeycomb lattice (see Figure S5) is only slightly changed when the quantum effects of $S=1$ are taken into account.[S38] Since our magnetic model for NiPS$_3$ is well-separated from any of those phase boundaries (see Figure S5b), the stability of the zigzag antiferromagnetic phase, which is the low temperature phase of monolayer NiPS$_3$ given by the classical J_1-J_2-J_3 model, would not be affected by such small quantum fluctuation effects.
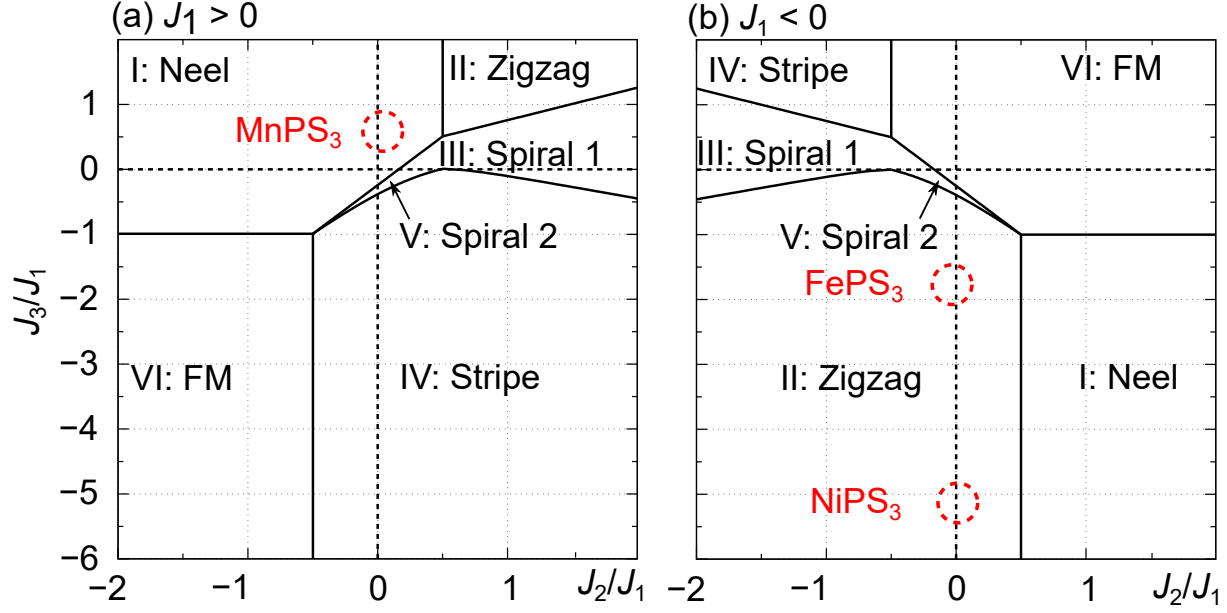
Figure S5: Phase diagrams of the classical J_1-J_2-J_3 model on the honeycomb lattice[S39,S40] for (a) $J_1 > 0$ for MnPS$_3$ and (b) $J_1 < 0$ for FePS$_3$ and NiPS$_3$.

For all these reasons, for monolayer NiPS$_3$, the classical J_1-J_2-J_3 model provides almost the same answer as the quantum ($S=1$) J_1-J_2-J_3 model. Our use of classical Monte Carlo simulation can be justified in this regard.

Because the magnitude of the isotropic intralayer exchange interaction is much larger than that of the other contributions (the anisotropic intralayer exchange interactions, the single-ion anisotropy, and the dipolar anisotropy), we expect that our conclusion given above will not change when those minor contributions are fully considered within the quantum version ($S=1$) of our magnetic model for NiPS$_3$.

References

(S1) Kurosawa, K.; Saito, S.; Yamaguchi, Y. Neutron Diffraction Study on MnPS$_3$ and FePS$_3$. *Journal of the Physical Society of Japan* **1983**, *52*, 3919–3926.

(S2) Lançon, D.; Walker, H. C.; Ressouche, E.; Ouladdiaf, B.; Rule, K. C.; McIntyre, G. J.;

Hicks, T. J.; Rønnow, H. M.; Wildes, A. R. Magnetic Structure and Magnon Dynamics of the Quasi-Two-Dimensional Antiferromagnet FePS$_3$. *Phys. Rev. B* **2016**, *94*, 214407.

(S3) Wildes, A. R.; Simonet, V.; Ressouche, E.; McIntyre, G. J.; Avdeev, M.; Suard, E.; Kimber, S. A. J.; Lançon, D.; Pepe, G.; Moubaraki, B.; Hicks, T. J. Magnetic Structure of the Quasi-Two-Dimensional Antiferromagnet NiPS$_3$. *Phys. Rev. B* **2015**, *92*, 224408.

(S4) Giannozzi, P.; Baroni, S.; Bonini, N.; Calandra, M.; Car, R.; Cavazzoni, C.; Ceresoli, D.; Chiarotti, G. L.; Cococcioni, M.; Dabo, I.; Corso, A. D.; de Gironcoli, S.; Fabris, S.; Fratesi, G.; Gebauer, R.; Gerstmann, U.; Gougoussis, C.; Kokalj, A.; Lazzeri, M.; Martin-Samos, L.; Marzari, N.; Mauri, F.; Mazzarello, R.; Paolini, S.; Pasquarello, A.; Paulatto, L.; Sbraccia, C.; Scandolo, S.; Sclauzero, G.; Seitsonen, A. P.; Smogunov, A.; Umari, P.; Wentzcovitch, R. M. QUANTUM ESPRESSO: A Modular and Open-Source Software Project for Quantum Simulations of Materials. *J. Phys.: Condens. Matter* **2009**, *21*, 395502.

(S5) Ma, P.-W.; Dudarev, S. L. Constrained Density Functional for Noncollinear Magnetism. *Phys. Rev. B* **2015**, *91*, 054420.

(S6) Perdew, J. P.; Zunger, A. Self-Interaction Correction to Density-Functional Approximations for Many-Electron Systems. *Phys. Rev. B* **1981**, *23*, 5048–5079.

(S7) Liechtenstein, A. I.; Anisimov, V. I.; Zaanen, J. Density-Functional Theory and Strong Interactions: Orbital Ordering in Mott-Hubbard Insulators. *Phys. Rev. B* **1995**, *52*, R5467–R5470.

(S8) Timrov, I.; Marzari, N.; Cococcioni, M. Hubbard Parameters from Density-Functional Perturbation Theory. *Phys. Rev. B* **2018**, *98*, 085127.

(S9) Aryasetiawan, F.; Karlsson, K.; Jepsen, O.; Schönberger, U. Calculations of Hubbard U from First-Principles. *Phys. Rev. B* **2006**, *74*, 125106.

(S10) Hamann, D. R. Optimized Norm-Conserving Vanderbilt Pseudopotentials. *Phys. Rev. B* **2013**, *88*, 085117.

(S11) Schlipf, M.; Gygi, F. Optimization Algorithm for the Generation of ONCV Pseudopotentials. *Comput. Phys. Commun.* **2015**, *196*, 36–44.

(S12) Ouvrard, G.; Brec, R.; Rouxel, J. Structural Determination of Some MPS_3 Layered Phases (M = Mn, Fe, Co, Ni and Cd). *Mater. Res. Bull.* **1985**, *20*, 1181–1189.

(S13) Solovyev, I. V.; Mazurenko, V. V.; Katanin, A. A. Validity and Limitations of the Superexchange Model for the Magnetic Properties of Sr_2IrO_4 and Ba_2IrO_4 Mediated by the Strong Spin-Orbit Coupling. *Phys. Rev. B* **2015**, *92*, 235109.

(S14) Fang, Z.; Nagaosa, N. Quantum versus Jahn-Teller Orbital Physics in YVO_3 and $LaVO_3$. *Phys. Rev. Lett.* **2004**, *93*, 176404.

(S15) Yaresko, A. N.; Liu, G.-Q.; Antonov, V. N.; Andersen, O. K. Interplay between Magnetic Properties and Fermi Surface Nesting in Iron Pnictides. *Phys. Rev. B* **2009**, *79*, 144421.

(S16) Jacobsson, A.; Sanyal, B.; Ležaić, M.; Blügel, S. Exchange Parameters and Adiabatic Magnon Energies from Spin-Spiral Calculations. *Phys. Rev. B* **2013**, *88*, 134427.

(S17) Foyevtsova, K.; Jeschke, H. O.; Mazin, I. I.; Khomskii, D. I.; Valentí, R. Ab Initio Analysis of the Tight-Binding Parameters and Magnetic Interactions in Na_2IrO_3. *Phys. Rev. B* **2013**, *88*, 035107.

(S18) Lambrecht, W. R. L.; Prikhodko, M.; Miao, M. S. Electronic Structure and Magnetic Interactions in MnN and Mn_3N_2. *Phys. Rev. B* **2003**, *68*, 174411.

(S19) Kim, K.; Lim, S. Y.; Lee, J.-U.; Lee, S.; Kim, T. Y.; Park, K.; Jeon, G. S.; Park, C.-H.; Park, J.-G.; Cheong, H. Suppression of Magnetic Ordering in XXZ-Type Antiferromagnetic Monolayer $NiPS_3$. *Nat. Commun.* **2019**, *10*, 345.

(S20) Monkhorst, H. J.; Pack, J. D. Special Points for Brillouin-Zone Integrations. *Phys. Rev. B* **1976**, *13*, 5188–5192.

(S21) Hobbs, D.; Kresse, G.; Hafner, J. Fully Unconstrained Noncollinear Magnetism within the Projector Augmented-Wave Method. *Phys. Rev. B* **2000**, *62*, 11556–11570.

(S22) Scalmani, G.; Frisch, M. J. A New Approach to Noncollinear Spin Density Functional Theory beyond the Local Density Approximation. *J. Chem. Theory Comput.* **2012**, *8*, 2193–2196.

(S23) The Elk Code (https://elk.sourceforge.io).

(S24) Kresse, G.; Furthmüller, J. Efficient Iterative Schemes for Ab Initio Total-Energy Calculations Using a Plane-Wave Basis Set. *Phys. Rev. B* **1996**, *54*, 11169–11186.

(S25) Eich, F. G.; Pittalis, S.; Vignale, G. Transverse and Longitudinal Gradients of the Spin Magnetization in Spin-Density-Functional Theory. *Phys. Rev. B* **2013**, *88*, 245102.

(S26) Desmarais, J. K.; Flament, J.-P.; Erba, A. Spin-Orbit Coupling from a Two-Component Self-Consistent Approach. I. Generalized Hartree-Fock Theory. *J. Chem. Phys.* **2019**, *151*, 074107.

(S27) Desmarais, J. K.; Flament, J.-P.; Erba, A. Retraction: "Spin-Orbit Coupling from a Two-Component Self-Consistent Approach. II. Non-Collinear Density Functional Theories" [J. Chem. Phys. 151, 074108 (2019)]. *J. Chem. Phys.* **2021**, *154*, 159901.

(S28) Joy, P. A.; Vasudevan, S. Magnetism in the Layered Transition-Metal Thiophosphates MPS_3 (M=Mn, Fe, and Ni). *Phys. Rev. B* **1992**, *46*, 5425–5433.

(S29) Liechtenstein, A. I.; Katsnelson, M. I.; Antropov, V. P.; Gubanov, V. A. Local Spin Density Functional Approach to the Theory of Exchange Interactions in Ferromagnetic Metals and Alloys. *J. Magn. Magn. Mater.* **1987**, *67*, 65–74.

(S30) Nauman, M.; Kiem, D. H.; Lee, S.; Son, S.; Park, J.-G.; Kang, W.; Han, M. J.; Jo, Y. Complete Mapping of Magnetic Anisotropy for Prototype Ising van Der Waals $FePS_3$. *2D Mater.* **2021**, *8*, 035011.

(S31) Olsen, T. Magnetic Anisotropy and Exchange Interactions of Two-Dimensional FePS3, NiPS3 and MnPS3 from First Principles Calculations. *Journal of Physics D: Applied Physics* **2021**, *54*, 314001.

(S32) Perdew, J. P.; Burke, K.; Ernzerhof, M. Generalized Gradient Approximation Made Simple. *Phys. Rev. Lett.* **1996**, *77*, 3865–3868.

(S33) Chittari, B. L.; Park, Y.; Lee, D.; Han, M.; MacDonald, A. H.; Hwang, E.; Jung, J. Electronic and Magnetic Properties of Single-Layer MPX_3 Metal Phosphorous Trichalcogenides. *Phys. Rev. B* **2016**, *94*, 184428.

(S34) Metropolis, N.; Rosenbluth, A. W.; Rosenbluth, M. N.; Teller, A. H.; Teller, E. Equation of State Calculations by Fast Computing Machines. *J. Chem. Phys.* **1953**, *21*, 1087–1092.

(S35) Wolff, U. Collective Monte Carlo Updating for Spin Systems. *Phys. Rev. Lett.* **1989**, *62*, 361–364.

(S36) D'Onorio De Meo, M.; Oh, S. K. Wolff Algorithm and Anisotropic Continuous-Spin Models: An Application to the Spin–van Der Waals Model. *Phys. Rev. B* **1992**, *46*, 257–260.

(S37) Leblanc, M. D.; Whitehead, J. P.; Plumer, M. L. Monte Carlo Simulations of Intragrain Spin Effects in a Quasi-2D Heisenberg Model with Uniaxial Anisotropy. *J. Phys.: Condens. Matter* **2013**, *25*, 196004.

(S38) Merino, J.; Ralko, A. Role of Quantum Fluctuations on Spin Liquids and Ordered Phases in the Heisenberg Model on the Honeycomb Lattice. *Phys. Rev. B* **2018**, *97*, 205112.

(S39) Rastelli, E.; Tassi, A.; Reatto, L. Non-Simple Magnetic Order for Simple Hamiltonians. *Physica B+C* **1979**, *97*, 1–24.

(S40) Fouet, J.; Sindzingre, P.; Lhuillier, C. An Investigation of the Quantum J_1-J_2-J_3 Model on the Honeycomb Lattice. *Eur. Phys. J. B* **2001**, *20*, 241–254.